

Anisotropic damage evolution in shock wave-loaded viscoplastic plates

M. STOFFEL

*Institut für Allgemeine Mechanik, RWTH Aachen
Templergraben 64, 52056 Aachen, Germany
e-mail: stoffel@iam.rwth-aachen.de*

IN THE DESIGN of structural elements, which are used for protection against explosions, the damage evolution until failure has to be predicted in numerical simulations. However, in the literature a wide variety of damage models is available based on different approaches, e.g. phenomenological and micromechanical theories. Furthermore, the consequences of connections between new damage models and the constitutive equations accounting for elastic-viscoplasticity are unclear. The same problem occurs if structural theories, involving hypotheses, are combined with damage laws. In order to verify the calculated results, experiments with structures subjected to pressure waves are necessary. For this reason, an experimental validation method by means of shock tubes is used in the present study to verify the isotropic and anisotropic damage models. The measured deformations and experimentally observed failure modes can then be compared to the simulated results.

Key words: damage; dynamics; shock waves; viscoplasticity.

1. Introduction

IN ORDER TO VALIDATE the calculated results, two shock tubes are used in this study. In the experiments, initially flat circular metal plates are subjected to plane pressure waves. Displacements of the plates and the pressure acting on the specimens are recorded during the impulse period in time ranges of microseconds by means of short time measurement technique. In a preliminary study [1] this technique was introduced and several examples for validation studies concerning viscoplastic constitutive equations were given. In the present investigation, this technique is extended to damage and failure problems. The aim is to determine by means of comparisons between experiments and simulations, how precise the damage growth and the failure of shock wave-loaded plates can be predicted in finite element calculations.

In order to cause a rupture of the plate after one impulsive loading or after repeated loadings on the same side of the plate, large deflections and large strains would be necessary due to the ductile behaviour of the material used. But in this case, a not negligible fluid-structure interaction would occur. If these

fluid mechanical influences were taken into account in the simulations, it could not be verified, if e.g. differences between experiments and calculations would be caused by shortcomings in the structural modelling or in the fluid mechanical description. For this reason, an alternate deformation case is applied to the shock wave-loaded plates, which causes damage until rupture in a region of moderate deflections. The small fluid-structure-interaction which can occur during the experiments is neglected in the simulations of this study. The alternate deformation behaviour of inelastically deformed plates causes the problem of buckling, i.e. the type of snap-through has to be determined experimentally. The buckling process can be rotationally symmetrical or unsymmetrical. The type of snap-through will be clarified experimentally later in this investigation.

During alternate shock wave loadings a damage growth occurs in the considered aluminium plates. However, if cyclic loading processes are regarded, leading to damage due to alternate loadings, damage laws could be applied which account for damage evolutions depending on the loading cycles, e.g. fatigue laws. Consequently, material parameters for this kind of damage would be necessary and must be determined from material tests. But in the present study, compression tests are neglected due to the danger of buckling of the specimens. Therefore, a material law accounting for cyclic damage cannot be applied here but a model which calculates a damage growth depending on the plastic strain should be chosen. In recent years, a lot of studies about new damage laws were published which are applicable for metal materials. Based on the effective stress concept of LEMAITRE and CHABOCHE [2], a damage evolution law of LEMAITRE *et al.* [3] was presented with a damage tensor accounting for independent damage evolution in three coordinate directions. Other phenomenological theories which cover mathematically the loss of stiffness of damaged material, were e.g. proposed by CHOW and WANG [4] who used a damage effect tensor for deriving anisotropic damage evolution equations. In a study of LUBARDA and KRAJCI-NOVIC [5] material degradation due to damage and induced elastic anisotropy is introduced by a damage tensor. Further investigations followed by BIEGLER and MEHRABADI [6], MAROTTI DE SCIARRA [7], QI and BERTRAM [8], KUHL and RAMM [9], CAROL *et al.* [10]. MENZEL and STEINMANN [11] proposed a theoretical and computational model for the treatment of anisotropic damage at large strains. AL-RUB and VOYIADJIS [12] derived an anisotropic damage model coupled to elastic-plasticity based on the effective stress concept. STUMPF *et al.* [13] proposed a nonlocal gradient damage theory for finite strains. VOYIADJIS *et al.* [14] introduced a general elastic-viscoplastic material law coupled to rate-dependent damage. This viscodamage model is derived in the framework of a gradient theory. MENZEL *et al.* [15] coupled viscoplasticity to anisotropic continuum damage and introduced a so-called tangent map to account for anisotropic properties. A consistent theory for anisotropic continuum mechanics was developed

by BRÜNIG and RICCI [16] who introduced a nonlocal yield condition of the Drucker-Prager type.

Due to the microscopic effects which cause a damage growth, scientists have developed damage laws based on micromechanical approaches. A comparative study between phenomenological and micromechanical aspects was presented by VOYIADJIS and THIAGARAJAN [14]. Further comparisons between a macromechanical description of damage and an approach on a meso-scale level were drawn by LEUKART and RAMM [17] and numerical examples were given. EKH *et al.* [18] developed a model framework for anisotropic damage coupled to crystal viscoplasticity for finite strains.

These different approaches show different possibilities how to treat the damage evolution and which can lead, consequently, to different results in calculations. In the present study a fundamental phenomenological law is chosen for the numerical simulations: the anisotropic damage law of LEMAITRE *et al.* [3] which allows to determine the material parameters from tension tests with loading and unloading cycles.

2. Mechanical model

2.1. Constitutive equations

Based on the stress equivalence principle, the effective stress in a damaged continuum can be written for the isotropic case as

$$(2.1) \quad \tilde{\sigma}_{ij} = \frac{\sigma_{ij}}{1 - D}.$$

The damage evolution in a three-dimensional continuum is in [2] expressed by

$$(2.2) \quad \dot{D} = \frac{D_c}{\varepsilon_R - \varepsilon_D} \left[\frac{2}{3}(1 + \nu) + 3(1 - 2\nu) \left(\frac{\sigma_H}{\sigma_{eq}} \right)^2 \right] \dot{p},$$

where \dot{D} , D_c , ε_R , ε_D , ν , σ_h , σ_{eq} , \dot{p} stand for the damage increment, the critical damage, the critical plastic strain, the damage threshold strain, Poisson's ratio, hydrostatic stress, equivalent von Mises stress, equivalent plastic strain rate. The term in angular brackets is responsible for a multi-axial loading which can accelerate the damage growth. In the material parameter identification process the loss of elastic stiffness is covered by a diminishing Young's modulus in the form

$$(2.3) \quad \tilde{E} = E \cdot (1 - D).$$

In this way, the damage can be determined with respect to the plastic strain. Applied to Eq. (2.2) the term in angular brackets becomes 1 in the case of

the tension tests and the material parameters in front of the brackets can be determined by curve fitting.

In the anisotropic damage law three different damage variables are introduced which cover the development of material damage independently in three coordinate directions. These three variables do not depend on the equivalent plastic strain anymore, which represents an isotropic value, but on the absolute value of the plastic normal strain in the corresponding directions. In the next section the damage law is adapted to the hypotheses of the shell theory used.

For a damage growth description in three coordinate directions, the damage tensor was introduced in [3] in the form:

$$(2.4) \quad D_{ij} = \begin{bmatrix} D_1 & 0 & 0 \\ 0 & D_2 & 0 \\ 0 & 0 & D_3 \end{bmatrix}.$$

Here, it is assumed that the principal directions of the damage, stress and strain tensor are the same. The result of this applied damage tensor is that damage growth can occur in three different coordinate directions separately. This material model is necessary in this study to predict the anisotropic nature of a crack. The deviatoric part of an undamaged deviatoric stress tensor is defined as

$$(2.5) \quad \sigma_{ij}^D = \sigma_{ij} - \sigma_H \delta_{ij} \quad \text{with} \quad \sigma_H = \frac{1}{3} \sigma_{kk}.$$

Using the Gibbs energy for linear and initially isotropic elasticity for the damaged material

$$(2.6) \quad \rho\psi^* = \frac{1+\nu}{2E} H_{ij} \sigma_{jk}^D H_{kl} \sigma_{li}^D + \frac{3(1-2\nu)}{2E} \frac{\sigma_H^2}{1-D_H},$$

the effective stress tensor $\tilde{\sigma}_{ij}$ is expressed by:

$$(2.7) \quad \tilde{\sigma}_{ij} = H_{ik} \sigma_{kl}^D H_{lj} + \frac{\sigma_H}{1-D_H} \delta_{ij}.$$

Here, the tensor H_{ij} is equal to

$$(2.8) \quad H_{ij} = \frac{1}{\sqrt{1-D_{ij}}} = \begin{bmatrix} \frac{1}{\sqrt{1-D_1}} & 0 & 0 \\ 0 & \frac{1}{\sqrt{1-D_2}} & 0 \\ 0 & 0 & \frac{1}{\sqrt{1-D_3}} \end{bmatrix}$$

and

$$(2.9) \quad D_H = \frac{1}{3} D_{kk} = \frac{1}{3} (D_1 + D_2 + D_3)$$

denoting the hydrostatic part of the damage tensor D_{ij} . The anisotropic nature of void growth is covered by the evolution of the damage parameters D_i independently of each other.

The effective stress tensor $\tilde{\sigma}_{ij}$ in Eq. (2.7) is decomposed into the effective deviatoric and the hydrostatic stress tensor

$$(2.10) \quad \tilde{\sigma}_{ij}^D = H_{ik}\sigma_{kl}^D H_{ij}, \quad \tilde{\sigma}_H = \frac{\sigma_H}{1 - D_H} \delta_{ij},$$

respectively. Here, the value D_H represents an average amount of damage. This separation becomes clear, if we regard e.g. the one-dimensional case with $\sigma_{11} = \sigma$ and $\sigma_H = \frac{1}{3}\sigma$ as well as $\sigma_{11}^D = \frac{2}{3}\sigma$; $\sigma_{22}^D = \sigma_{33}^D = -\frac{1}{3}\sigma$. Then, it follows from Eq. (2.7):

$$(2.11) \quad \tilde{\sigma}_{11}^D = H_{1k}\sigma_{kl}^D H_{l1} = H_{11}\sigma_{l1}^D H_{l1} = H_{11}\sigma_{11}^D H_{11} = \frac{\sigma_{11}^D}{1 - D_1}$$

with all components $H_{ij} = 0$ and $\sigma_{ij}^D = 0$ for $i \neq j$. Together with the hydrostatic part, the effective stress becomes

$$(2.12) \quad \tilde{\sigma}_{11} = \frac{2}{3} \cdot \frac{\sigma}{1 - D_1} + \frac{1}{3} \cdot \frac{\sigma}{1 - (D_1 + D_2 + D_3)/3}.$$

In the special case of isotropic damage, i.e. if the damage evolution is the same in each coordinate direction ($D_1 = D_2 = D_3 = D$), the effective stress tensor could be reduced to $\tilde{\sigma}_{11} = \sigma/(1 - D)$.

In order to account for viscoplasticity, the anisotropic damage model is combined with the viscoplastic law of LEMAITRE and CHABOCHE [2] and Hooke's law, assuming

$$(2.13) \quad \dot{\epsilon}_{ij} = \dot{\epsilon}_{ij}^e + \dot{\epsilon}_{ij}^p = \frac{1 + \nu}{E} \tilde{\sigma}_{ij} - \frac{\nu}{E} \tilde{\sigma}_{kk} \delta_{ij} + \dot{\epsilon}_{ij}^p.$$

The plastic strain rate is expressed by a modification of the viscoplastic law in [2] which is introduced by LEMAITRE *et al.* [3] as

$$(2.14) \quad \dot{\epsilon}_{ij}^p = \frac{3}{2} \frac{[H_{ik}(\tilde{\sigma}_{kl}^D - X_{kl})H_{lj}]^D}{[H_{ik}(\tilde{\sigma}_{kl}^D - X_{kl})H_{lj}]_{eq}} \dot{p},$$

with $[\sigma_{ij}]_{eq}$ denoting the second invariant $\sqrt{\frac{3}{2}\sigma_{ij}\sigma_{ij}}$ of a tensor σ_{ij} . Due to the fact that only tension tests and no compression tests are used in the present study, pure kinematic hardening is assumed in the form

$$(2.15) \quad \dot{X}_{ij} = \frac{2}{3} C \dot{\beta}_{ij} - \gamma X_{ij} \dot{r}$$

with

$$(2.16) \quad \dot{r} = \frac{(\tilde{\sigma}_{ij}^D - X_{ij})_{eq}}{[H_{ik}(\tilde{\sigma}_{kl}^D - X_{kl})H_{lj}]_{eq}} \dot{p}$$

and

$$(2.17) \quad \dot{\beta}_{ij} = \frac{3}{2} \dot{r} \frac{\tilde{\sigma}_{ij}^D - X_{ij}}{(\tilde{\sigma}_{ij}^D - X_{ij})_{eq}} = \frac{3}{2} \dot{p} \frac{\tilde{\sigma}_{ij}^D - X_{ij}}{[H_{ik}(\tilde{\sigma}_{kl}^D - X_{kl})H_{lj}]_{eq}}.$$

In the present work, the combination between the anisotropic damage law and the viscoplastic model is carried out by using here the equivalent plastic strain rate from the original law of LEMAITRE and CHABOCHE [2]:

$$(2.18) \quad \dot{p} = \left\langle \frac{(\tilde{\sigma}_{ij}^D - X_{ij})_{eq} - k}{K} \right\rangle^n.$$

In Eq. (2.18) the connection of the viscoplastic law and the damage evolution is included in the effective stress tensor.

The anisotropic evolution law for the principal values of the damage tensor reads

$$(2.19) \quad \dot{D}_{ij} = \frac{D_c}{\varepsilon_R - \varepsilon_D} \left[\frac{2}{3}(1 + \nu) + 3(1 - 2\nu) \left(\frac{\sigma_h}{\sigma_{eq}} \right)^2 \right] |\dot{\varepsilon}^p|_{ij}.$$

For the finite element programming, it is necessary to determine the tensors in Eqs. (2.14), (2.16)–(2.18) which include the effective deviatoric stress and the backstress:

$$(2.20) \quad \tilde{\sigma}_{ij}^D - X_{ij} = H_{ik} \sigma_{kl}^D H_{lj} - X_{ij}$$

$$= \begin{bmatrix} \frac{\sigma_{11}^D}{1-D_1} - X_{11} & \frac{\sigma_{12}^D}{\sqrt{(1-D_1)(1-D_2)}} - X_{12} & \frac{\sigma_{13}^D}{\sqrt{(1-D_1)(1-D_3)}} - X_{13} \\ \frac{\sigma_{12}^D}{\sqrt{(1-D_1)(1-D_2)}} - X_{12} & \frac{\sigma_{22}^D}{1-D_2} - X_{22} & \frac{\sigma_{23}^D}{\sqrt{(1-D_2)(1-D_3)}} - X_{23} \\ \frac{\sigma_{13}^D}{\sqrt{(1-D_1)(1-D_3)}} - X_{13} & \frac{\sigma_{23}^D}{\sqrt{(1-D_2)(1-D_3)}} - X_{23} & \frac{\sigma_{33}^D}{1-D_3} - X_{33} \end{bmatrix}.$$

From the tensor in Eq. (2.20) it can be seen that also the components accounting for the shear stresses are affected by the damage growth. This makes physically sense, because due to the loss of a load carrying cross-section area the

shear stiffness is weakened. This effect is described mathematically by the effective shear stresses. In Eq. (2.14) the tensor from Eq. (2.20) is again multiplied by H_{ik} . The resulting tensor reads

$$(2.21) \quad H_{ik}(\tilde{\sigma}_{kl}^D - X_{kl})H_{lj} = \begin{bmatrix} \frac{\tilde{\sigma}_{11}^D - X_{11}}{1 - D_1} & \frac{\tilde{\sigma}_{12}^D - X_{12}}{\sqrt{(1 - D_1)(1 - D_2)}} & \frac{\tilde{\sigma}_{13}^D - X_{13}}{\sqrt{(1 - D_1)(1 - D_3)}} \\ \frac{\tilde{\sigma}_{12}^D - X_{12}}{\sqrt{(1 - D_1)(1 - D_2)}} & \frac{\tilde{\sigma}_{22}^D - X_{22}}{1 - D_2} & \frac{\tilde{\sigma}_{23}^D - X_{23}}{\sqrt{(1 - D_2)(1 - D_3)}} \\ \frac{\tilde{\sigma}_{13}^D - X_{13}}{\sqrt{(1 - D_1)(1 - D_3)}} & \frac{\tilde{\sigma}_{23}^D - X_{23}}{\sqrt{(1 - D_2)(1 - D_3)}} & \frac{\tilde{\sigma}_{33}^D - X_{33}}{1 - D_3} \end{bmatrix}$$

and exhibits also effective shear stress values. The numerical model used is based on a shell theory which neglects thickness change and consequently the plastic strain ε_{33}^p . Due to the fact that the ductile damage depends on the plastic strain, the damage parameter D_3 in the above described equations is set to zero.

2.2. Structural theory and numerical approach

The structural behaviour of the investigated plates is covered by a geometrically non-linear first-order shear deformation theory. Details about the kinematic relations between strains and displacements can be found in [1, 19]. This theory turned out to be appropriate to predict structural deformations caused by shock waves and is therefore applied here. Furthermore, the source code for the finite element simulations is available which makes it possible to trace all calculation steps precisely.

The displacement vector in a three-dimensional continuum can be expressed by its components in the form described by

$$(2.22) \quad v_\alpha = v_\alpha^0 + \theta v_\alpha^1; \quad v_3 = v_3^0, \quad \alpha = 1, 2,$$

where v_α^0, v_3^0 denote the displacement components, v_α^1 are the rotations at the midsurface, and θ is the normal coordinate. In order to trace the evolution of each material parameter in the shell space, the shell is divided into layers. The volumetric response of the structure is transformed into a two-dimensional description by applying the displacement vector from Eq. (2.22) to the Green–Lagrange strain tensor. According to small strains and moderate rotations, the general Green–Lagrange strain tensor in the shell space = 1, 2, 3 can be expressed by

$$(2.23) \quad \varepsilon_{\alpha\beta} = \overset{0}{\varepsilon}_{\alpha\beta} + \theta \overset{1}{\varepsilon}_{\alpha\beta} + \theta^2 \overset{2}{\varepsilon}_{\alpha\beta},$$

$$(2.24) \quad \varepsilon_{\alpha 3} = \overset{0}{\varepsilon}_{\alpha 3} + \theta \overset{1}{\varepsilon}_{\alpha 3},$$

$$(2.25) \quad \varepsilon_{33} = \overset{0}{\varepsilon}_{33},$$

with

$$(2.26) \quad \overset{0}{\varepsilon}_{\alpha\beta} = \overset{0}{\theta}_{\alpha\beta} + \frac{1}{2} \overset{0}{\varphi}_{\alpha} \overset{0}{\varphi}_{\beta},$$

$$(2.27) \quad \overset{1}{\varepsilon}_{\alpha\beta} = \frac{1}{2} (\overset{1}{v}_{\alpha|\beta} + \overset{1}{v}_{\beta|\alpha}) - \frac{1}{2} (b_{\alpha}^{\lambda} \overset{0}{\varphi}_{\lambda\beta} + b_{\beta}^{\lambda} \overset{0}{\varphi}_{\lambda\alpha}) \\ + \frac{1}{2} (\overset{0}{\varphi}_{\alpha} b_{\beta}^{\lambda} \overset{1}{v}_{\lambda} + \overset{0}{\varphi}_{\beta} b_{\alpha}^{\lambda} \overset{1}{v}_{\lambda}),$$

$$(2.28) \quad \overset{2}{\varepsilon}_{\alpha\beta} = -\frac{1}{2} (b_{\alpha}^{\lambda} \overset{1}{v}_{\lambda|\beta} + b_{\beta}^{\lambda} \overset{1}{v}_{\lambda|\alpha}) + \frac{1}{2} b_{\alpha}^{\lambda} b_{\beta}^{\kappa} \overset{1}{v}_{\lambda} \overset{1}{v}_{\kappa},$$

$$(2.29) \quad \overset{0}{\varepsilon}_{\alpha 3} = \frac{1}{2} (\overset{0}{\varphi}_{\alpha} + \overset{1}{v}_{\alpha}) + \frac{1}{2} \overset{1}{v}^{\lambda} \overset{0}{\varphi}_{\lambda\alpha},$$

$$(2.30) \quad \overset{1}{\varepsilon}_{\alpha 3} = \frac{1}{2} \overset{1}{v}^{\lambda} \overset{1}{v}_{\lambda|\alpha}, \quad \overset{0}{\varepsilon}_{33} = 0.$$

Here the abbreviations

$$(2.31) \quad \overset{0}{\theta}_{\alpha\beta} = \frac{1}{2} (\overset{0}{v}_{\alpha|\beta} + \overset{0}{v}_{\beta|\alpha}) - b_{\alpha\beta} \overset{0}{v}_3, \quad \overset{0}{\varphi}_{\alpha\beta} = \overset{0}{v}_{\alpha|\beta} - b_{\alpha\beta} \overset{0}{v}_3,$$

$$(2.32) \quad \overset{0}{\varphi}_{\alpha} = \overset{0}{v}_{3,\alpha} + b_{\alpha}^{\lambda} \overset{0}{v}_{\lambda},$$

have been used, where $b_{\alpha\beta}$ and b_{α}^{λ} denote the covariant and mixed components of the curvature tensor, while $(\cdot)_{|\alpha}$ denotes covariant differentiation with respect to the coordinate θ^{α} . Here the Einstein summation convention has been adopted with Greek indices from 1 to 2 and Latin indices from 1 to 3.

For the derivation of the equations of motion, the principle of virtual work for a continuous body is used in its general form

$$(2.33) \quad \int_{\mathcal{V}} [s^{ij} \delta \varepsilon_{ij}(\mathbf{V}) - \rho (F^i - A^i) \delta V_i] d\mathcal{V} - \int_{\mathcal{A}} (*s^i + D^i) \delta V_i d\mathcal{A} = 0.$$

Here s^{ij} are the components of the second Piola–Kirchhoff stress tensor, V_i are the components of the displacement vector, ρ denotes the mass density per unit volume of the undeformed body, F^i and A^i are the components of the body force and acceleration vector, $*s^i$ and D^i denote the components of the prescribed external stress vector and of the damping force vector (per unit area of the undeformed bounding surface \mathcal{A}) and \mathcal{V} is the volume of the body. For viscous damping the components of the damping force vector are proportional to the

velocity, i.e. they are given by $D^i = -D^{ij}\dot{V}_j$ with D^{ij} denoting the components of the damping tensor.

By inserting the above-described strain measurements into the general principle of virtual work Eq. (2.33), the three-dimensional structural behaviour is transformed into a 2-D formulation which leads to the equations of motion.

This resulting differential equation is solved numerically by means of the central difference method. For the integration of the constitutive equations the trapezoidal rule is used, i.e. the increments of the plastic strains, kinematic hardening parameter and damage at each time step are calculated as:

$$(2.34) \quad \Delta \boldsymbol{\varepsilon}_t^p = \frac{1}{2} \Delta t (\dot{\boldsymbol{\varepsilon}}_{t-\Delta t}^p + \dot{\boldsymbol{\varepsilon}}_t^{p,i}),$$

$$(2.35) \quad \Delta \mathbf{X}_t = \frac{1}{2} \Delta t (\dot{\mathbf{X}}_{t-\Delta t} + \dot{\mathbf{X}}_t^i),$$

$$(2.36) \quad \Delta D_t = \frac{1}{2} \Delta t (\dot{D}_{t-\Delta t} + \dot{D}_t^i).$$

The actual values are obtained by

$$(2.37) \quad \boldsymbol{\varepsilon}_t^p = \boldsymbol{\varepsilon}_t^{p,i} = \boldsymbol{\varepsilon}_{t-\Delta t}^p + \Delta \boldsymbol{\varepsilon}_t^p, \quad \mathbf{X}_t = \mathbf{X}_t^i = \mathbf{X}_{t-\Delta t} + \Delta \mathbf{X}_t,$$

$$(2.38) \quad D_t = D_t^i = D_{t-\Delta t} + \Delta D_t.$$

Here, i denotes the number of iterations.

3. Shock tube experiments and simulations

For the experiments two shock tubes were used and applied to copper plates of 138 mm and aluminium plates of 553 mm diameter. Displacements of the plate are measured with capacitive sensors, developed for this purpose, and the pressure acting on the plate is recorded by piezoelectric pressure devices. Both quantities are measured during the impulse duration. In order to perform cyclic experiments, copper and aluminium plates were clamped in the shock tubes.

In Fig. 1 a copper plate was subjected to a pressure impulse with a peak pressure of 20 bar. After unloading, the inelastically deformed plate was turned in the shock tube and subjected to the same impulsive loading again, causing a snap-through of the structure. In Fig. 1 the displacements, measured by four sensors, are presented during this snap-through. In the drawing the plate is shown with the four sensors in front of it. The time difference between two neighbouring measurement points is 1 μ s. The loading history is shown in Fig. 2. The centre deflection in Fig. 1 differs clearly from the three other values but between the measurements of the sensors 1,2 and 4 there is nearly no difference visible. The result is a rotational symmetry of the plate deformation during the

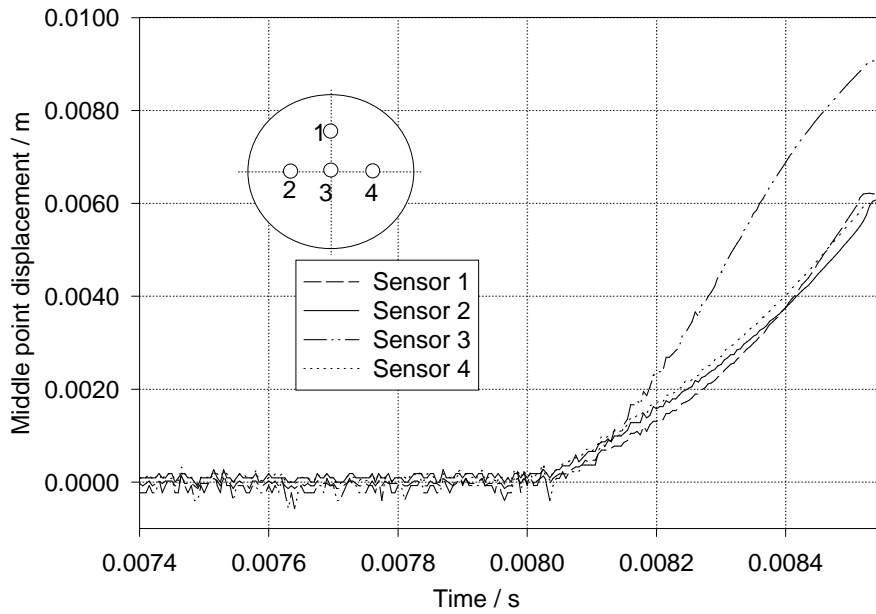


FIG. 1. Deflections of a copper plate during the first snap-through

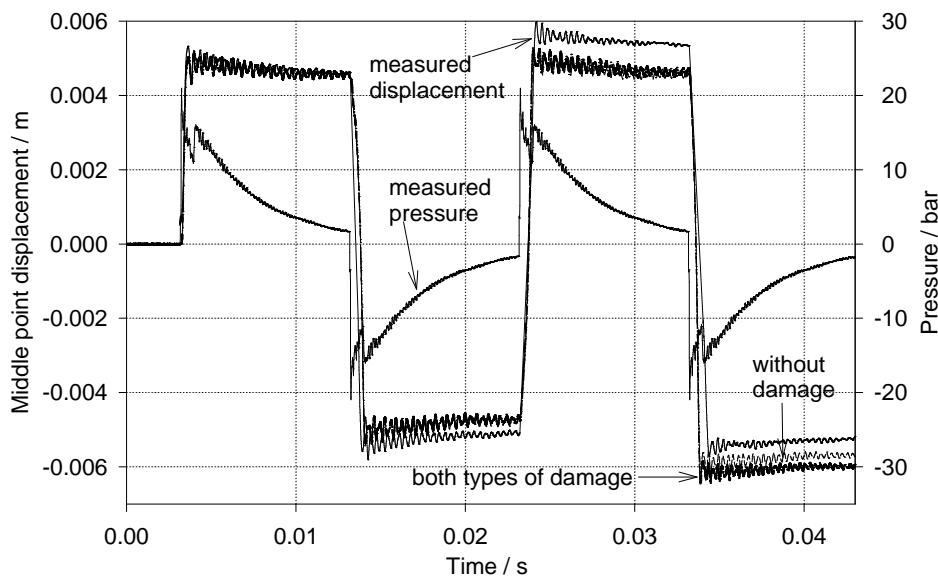


Fig. 2. Midpoint displacements of an alternately loaded copper plate (simulation and experiment)

snap-through. Based on this observation, the buckling of a shock wave-loaded plate in both tubes is assumed to be symmetrical in this study.

In Fig. 2 the measured and simulated plate deformations are presented which are caused by alternate shock wave loadings. A good agreement between the measured and numerically predicted plate deflections is observed. The measured and simulated curves are indicated in Fig. 2. With “both types of damage” it is indicated that simulations using isotropic and anisotropic damage lead to the same results.

Due to the alternate loading conditions, the plate specimens have to be clamped in additional ring flanges as it can be observed in Figs. 3. This clamping device is turned together with the plate after one shock wave load, otherwise the plate would deform due to residual stresses.



FIG. 3. Inelastic form of a snapped-through aluminium plate

In front of Fig. 3 an aluminium plate is shown which was subjected twice to shock waves. During the second impulsive loading a snap-through occurred. In [20] it was shown that, due to wave propagation phenomena, these aluminium plates exhibit a conical shape of the finally deformed structure after the first impulsive loading, see Fig. 4. The deformed plate in Fig. 3, which was loaded

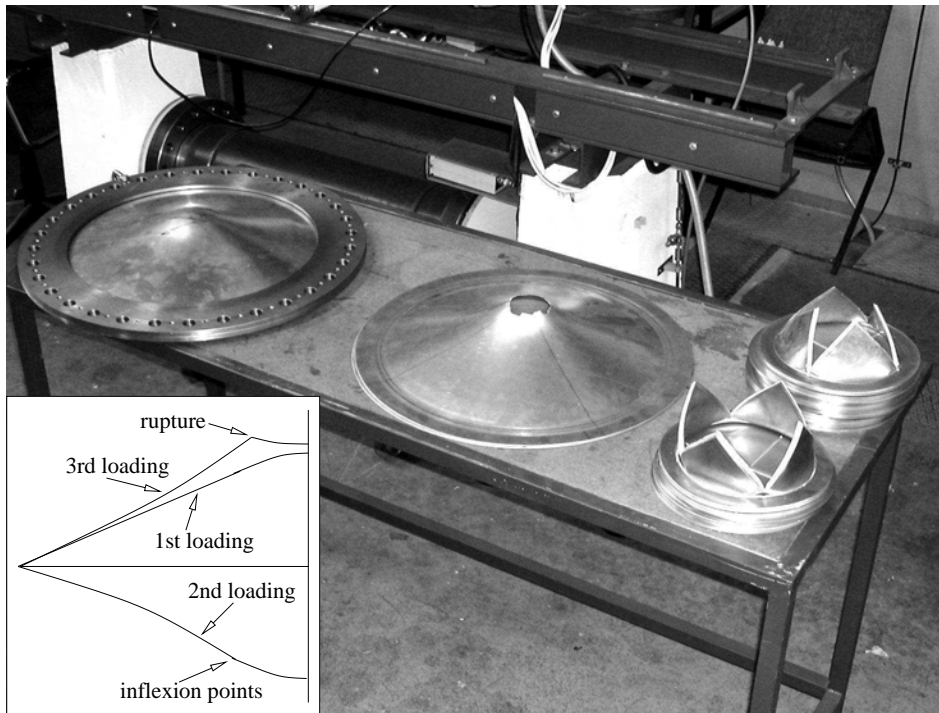


FIG. 4. Once and twice snapped-through aluminium plate with rupture as well as aluminium membranes used for these experiments

alternately from both sides, has a shape with two different curvature directions. Between the clamped area and the dashed line in Fig. 3 the plate is curved inwards and in the other area outwards. The dashed line denotes the locations of inflexion points on a circle with a radius of 5 cm. From this marked area towards the plate centre the surface material became very rough after the first snap-through. This can be an indication of evolution of voids in this area. In the background of Fig. 3 the originally undeformed aluminium plates are shown. After the third shock wave loading and the second snap-through, a circular piece of the plate breaks out. The ruptured plate is shown in the middle of Fig. 4. This hole with an average radius between 3 cm to 3.5 cm appears inside the area which was marked by the dashed line in Fig. 3. The permanent shapes of the aluminium plate after the three loadings are summarized in the drawing in Fig. 3 for the half of the plate. First, the conical shape is observed, after the second loading a circle of inflexion points is developed, and after the third loading the rupture occurs in this circular area. Thus, it was observed that this experimentally obtained failure mode of a circular hole was especially caused by the deformation history of the shock-wave loaded plate. In the case of a quasi-statically loaded

structure, a completely other kind of failure could occur. On the right-hand side in Fig. 4 aluminium membranes are shown which have been used during the experiments with aluminium plates. The experimentally obtained rupture can now be compared to simulations. Contrary to the experiments with copper plates, the centre deflection of the aluminium plate is not recorded, because the displacement sensor would be destroyed by the ruptured plate. Therefore, in Fig. 5 the measured pressure and the simulated deflections with and without damage, but no measured deflections, are shown. As described before, the snap-through is assumed to be symmetrical. The inelastic deformations with rotational symmetry in Figs. 3 and 4 support this condition. The calculated results in Fig. 5 of the damaged structure, using isotropic and anisotropic damage evolutions, are very similar to each other. It can be observed that the failure of the plate develops during the second snap-through, as it was observed in the experiment.

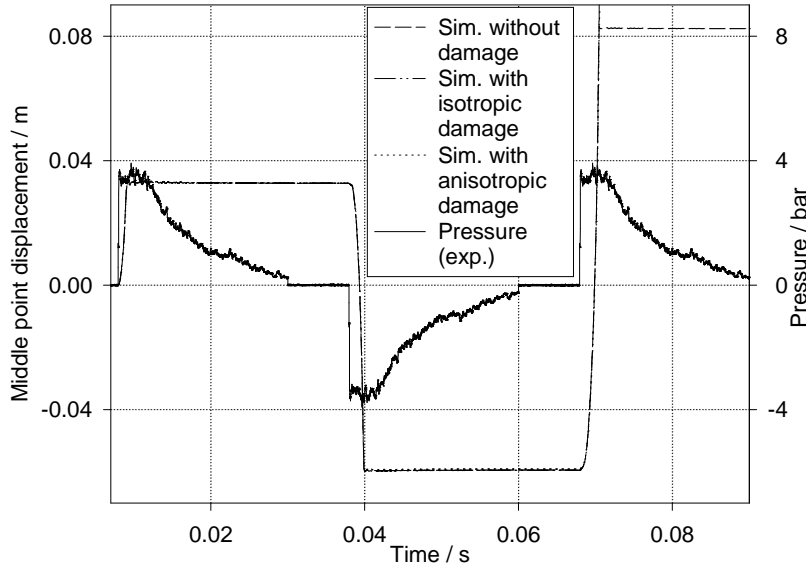


FIG. 5. Once and twice snapped-through aluminium plate with rupture as well as aluminium membranes used for these experiments

In Fig. 6 the damage evolution for the isotropic damage case is shown in several integration points in the bottom of the plate. Their distances to the plate centre are denoted 'r' in the legend. The critical damage is reached in the bottom of the plate centre already after the first snap-through. The damage amounts in the points with radii 3.5 cm, 4.4 cm and 6.1 cm are also close to the critical damage. But this prediction could not be confirmed in the experiment and the area of the above-described rough aluminium metal had a radius which was smaller than the simulated area of high damaged material. It means, that

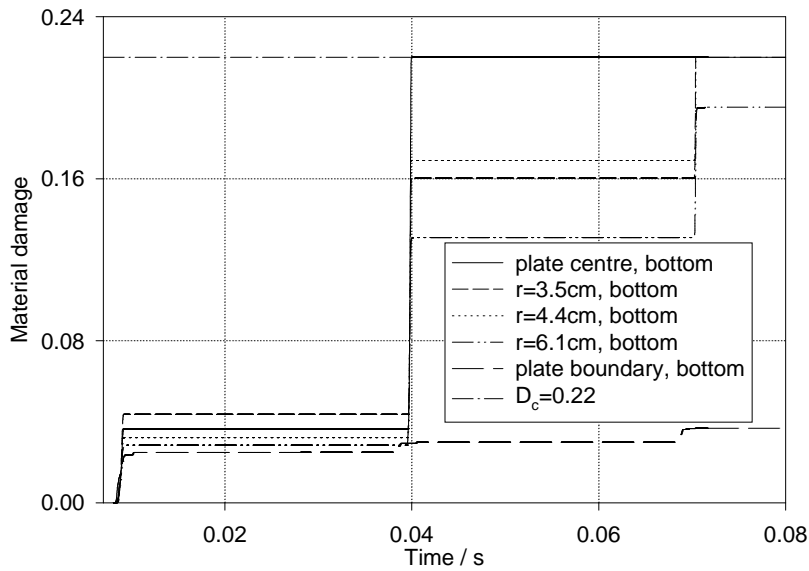


FIG. 6. Isotropic damage evolution in the bottom of the plate in different integration points

the damage growth is calculated too fast in this simulation. The prediction of structural failure is fulfilled, since the critical damage is predicted through the entire thickness at least in one location of the plate. This situation happens after the second snap-through in the plate centre, where the critical damage is also reached in all integration points, leading to the failure of the plate.

In Fig. 7 the damage evolution in the bottom of the plate in radial direction (D_1) is presented for the anisotropic case. Here, the damage growth is slower than in the isotropic formulation. The critical damage is not reached until the plate was loaded for the third time. This development leads to a much smaller damage after the second loading than in Fig. 6. After the second snap-through, not only the critical damage is reached in the midpoint but also the damage amount in a distance of 3.5 cm is close to the critical value of $D_c = 0.22$. In the midpoint the critical damage is obtained in all other layers, too. It is visible from Fig. 7 that the damage becomes much smaller, if distances to the centre of more than 3.5 cm are regarded. This prediction is in accordance with the experimentally obtained hole after the second snap-through and the observation that in the rest of the plate no damage was visible. At the boundary the damage remains very small. In Fig. 8 the damage evolution in circumferential direction (D_2) is shown. In the midpoint both damage values must be the same ($D_1 = D_2$). Also in this diagram the critical damage is reached in a distance of 3.5 cm from the midpoint after the rupture has occurred. However, after the plate has reached the critical amount of damage the simulation cannot be regarded as realistic

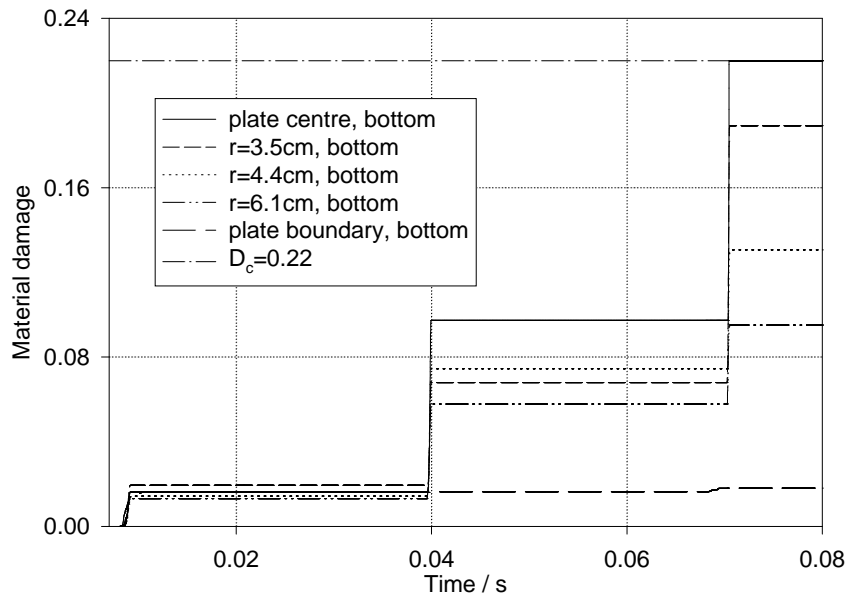


FIG. 7. Anisotropic damage evolution in radial direction (bottom of the plate in different integration points)

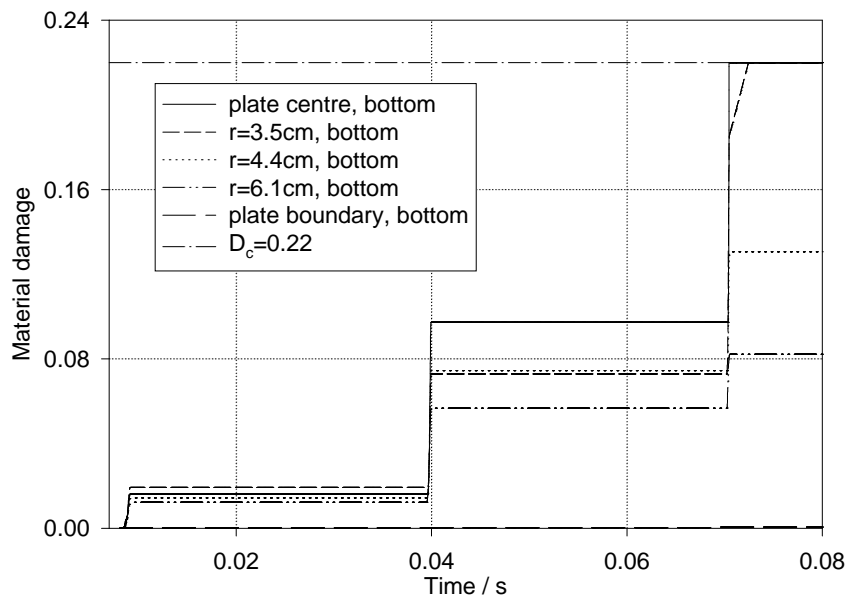


FIG. 8. Anisotropic damage evolution in circumferential direction (bottom of the plate in different integration points)

anymore. After the failure was obtained around the centre, causing a reduction of the Young's modulus to zero, the calculation in the surrounding elements is not relevant anymore.

The type of failure, represented by a hole in the plate, was able to predict in the simulation by an intensified damage growth in a circular area with a radius of 3.5 cm as indicated in Figs. 7 and 8. Furthermore, this failure mode was generated by the characteristic shape of the plate after the first snap-through in Fig. 3. In order to simulate this particular shape forming, it is necessary to use a material model which leads to a prediction of the wave propagation phenomena [20]. Due to different curvatures directions of the deformed plate shape, plastic strains are accumulated in a circular zone around the plate centre leading to a pronounced damage growth. For the prediction of this kind of failure caused by a hole in the plate centre, it was necessary to know the kind of snap-through, which was investigated by the short time measurements. This experimentally observed symmetric buckling was applied to the finite element simulations.

4. Conclusions

The presented validation method by means of shock tube experiments turned out to be appropriate to verify the simulated results. It was possible to create a reference state of a damaged and ruptured plate in the experiment with alternate loadings, which were compared to the predicted failures. It was shown that the inelastic shape forming of the structure has a significant influence on the type of failure in form of a hole in the deformed plate. For this reason, the choice of a structural model and of a viscoplastic law plays an equally important role as the use of an adequate damage law. Furthermore, it was possible to determine the rotational symmetric snap-through in the experiments by means of the applied short time measurement technique. In the numerical simulation the damage evolution and the failure were predicted most accurately by using the programmed anisotropic damage law.

References

1. M. STOFFEL, *A measurement technique for shock wave-loaded structures and its applications*, *Experimental Mechanics*, **46**, 47–55, 2006.
2. J. LEMAITRE, J.L. CHABOCHE, *Mechanics of Solid Materials*, Cambridge University Press, 1994.
3. J. LEMAITRE, R. DESMORAT, M. SAUZAY, *Anisotropic damage law of evolution*, *Eur. J. Mech. A/Solids*, **19**, 187–208, 2000.

4. C.L. CHOW, J. WANG, *An anisotropic theory of continuum damage mechanics for ductile fracture*, Engng. Frac. Mech., **27**, 5, 547–558, 1987.
5. V.A. LUBARDA, D. KRAJINOVIC, *Some fundamental issues in rate theory of damage-elastoplasticity*, Int. J. Plasticity, **11**, 7, 763–797, 1995.
6. M.W. BIEGLER, M.M. MEHRABADI, *An energy-based constitutive model for anisotropic solids subject to damage*, Mech. Mat., **19**, 2–3, 151–164, 1995.
7. F. MAROTTI DE SCIARRA, *A new variational theory and a computational algorithm for coupled elastoplastic damage models*, Int. J. Solids Structures, **34**, 14, 1761–1796, 1997.
8. W. QI, A. BERTRAM, *Anisotropic continuum damage modeling for single crystals at high temperatures*, Int. J. Plasticity, **15**, 11, 1197–1215, 1999.
9. E. KUHL, E. RAMM, *Simulation of strain localization with gradient enhanced damage models*, Comp. Mat. Sci., **16**, 1–4, 176–185, 1999.
10. I. CAROL, E. RIZZI, K. WILLAM, *On the formulation of anisotropic elastic degradation. I. Theory based on a pseudo-logarithmic damage tensor rate. II. Generalized pseudo-Rankine model for tensile damage*, Int. J. Solids Structures, **38**, 4, 491–546, 2001.
11. A. MENZEL, P. STEINMANN, *A theoretical and computational framework for anisotropic continuum damage mechanics at large strains*, Int. J. Solids Structures, **38**, 9505–9523, 2001.
12. R.K.A. AL-RUB, G.Z. VOYIADJIS, *On the coupling of anisotropic damage and plasticity models for ductile materials*, Int. J. Solids Structures, **40**, 11, 2611–2643, 2003.
13. H. STUMPF, J. MAKOWSKI, J. GORSKI, K. HACKL, *Thermodynamically consistent non-local theory of ductile damage*, Mech. Res. Comm., **31**, 355–363, 2004.
14. G.Z. VOYIADJIS, G. THIAGARAJAN, *Micro and macro anisotropic cyclic damage-plasticity models for MMCS.*, Int. J. Eng. Sci., **35**, 5, 467–484, 1997.
15. A. MENZEL, M. EKH, K. RUNESSON, P. STEINMANN, *A framework for multiplicative elastoplasticity with kinematic hardening coupled to anisotropic damage*, Int. J. Plasticity, **21**, 397–434, 2005.
16. M. BRÜNIG, S. RICCI, *Nonlocal continuum theory of anisotropically damaged metals*, Int. J. Plasticity, **21**, 1346–1382, 2005.
17. M. LEUKART, E. RAMM, *A comparison of damage models formulated on different material scales*, Comp. Mat. Sci., **28**, 749–762, 2003.
18. M. EKH, R. LILLBACKA, K. RUNESSON, *A model framework for anisotropic damage coupled to crystal (visco)plasticity*, Int. J. Plasticity, **20**, 2143–2159, 2004.
19. R. SCHMIDT, D. WEICHERT, *A refined theory of elastic-plastic shells at moderate rotations*, ZAMM, **69**, 11–21, 1989.
20. M. STOFFEL, *Shape forming of shock wave loaded viscoplastic plates*, Mech. Res. Comm., **33**, 35–41, 2006.

Received September 26, 2006; revised version July 15, 2008.
